
TENG-BC: Unified Time-Evolving Natural Gradient for Neural PDE Solvers with General Boundary Conditions

Hongjie Jiang¹ Di Luo^{2,3}

Abstract

Accurately solving time-dependent partial differential equations (PDEs) with neural networks remains challenging due to long-time error accumulation and the difficulty of enforcing general boundary conditions. We introduce TENG-BC, a high-precision neural PDE solver based on the Time-Evolving Natural Gradient, designed to perform under general boundary constraints. At each time step, TENG-BC performs a boundary-aware optimization that jointly enforces interior dynamics and boundary conditions, accommodating Dirichlet, Neumann, Robin, and mixed types within a unified framework. This formulation admits a natural-gradient interpretation, enabling stable time evolution without delicate penalty tuning. Across benchmarks over diffusion, transport, and nonlinear PDEs with various boundary conditions, TENG-BC achieves solver-level accuracy under comparable sampling budgets, outperforming conventional solvers and physics-informed neural network (PINN) baselines.

1. Introduction

Accurately and efficiently solving time-dependent partial differential equations (PDEs) remains a cornerstone challenge in computational science. Such equations govern a wide range of physical and engineering systems, from heat conduction and fluid transport to wave propagation, quantum dynamics, and reactive processes. Classical numerical solvers based on finite-difference, finite-element, and spectral methods achieve high accuracy through carefully designed discretizations and operator-specific schemes. However, their performance is tightly coupled to mesh quality, stencil design, and boundary handling.

¹School of Mathematical Sciences, Peking University, Beijing, China ²Department of Physics, Tsinghua University, Beijing, China ³Institute of Advanced Study, Tsinghua University, Beijing, China. Correspondence to: Di Luo <diluo1000@gmail.com>.

Recent years have witnessed rapid progress in neural-network-based PDE solvers (Han et al., 2017; Yu et al., 2018; Long et al., 2018; Carleo & Troyer, 2017; Raissi et al., 2019; Li et al., 2020; Lu et al., 2019; Sirignano & Spiliopoulos, 2018; Weinan et al., 2021; Chen et al., 2022; 2023b), which represent $u(x, t)$ by a neural network representation $u_\theta(x, t)$ and bypass explicit meshes. Despite their flexibility, most existing neural solvers face two recurring obstacles in time-dependent settings. (i) Global-in-time training: many approaches minimize a single space-time residual over $[0, T]$ (Raissi et al., 2019; Wang & Perdikaris, 2023; Wang et al., 2021b;a), which couples all time steps into one objective and provides weak control over local temporal errors; small global loss may still permit stepwise inaccuracies that propagate and amplify over time (Krishnapriyan et al., 2021; Wang et al., 2024). (ii) Boundary enforcement: physical boundary conditions are commonly handled by soft penalty terms (Raissi et al., 2019) that require careful weighting and often under-enforce Neumann, Robin or mixed boundaries. Alternatively, imposing hard boundary constraints that construct boundary-satisfying trial spaces (Lu et al., 2021; Sukumar & Srivastava, 2022) can be brittle for complex geometries, heterogeneous boundary segments, or time-dependent boundary data. These two issues compound in long-time simulations, where global objectives and imperfect boundary handling can jointly induce instability and reduce accuracy.

A promising remedy to the first issue is provided by the recently proposed *Time-Evolving Natural Gradient* (TENG) framework (Chen et al., 2024), which replaces global-in-time optimization by a sequence of localized, per-step functional projections. TENG achieves solver-level accuracy and strong long-time stability by controlling temporal evolution step by step. However, existing TENG formulations primarily focus on periodic or simple boundary settings.

Contributions. In this work, we present **TENG-BC**, a boundary-aware formulation of time-evolving neural PDE solvers that achieves high accuracy under general boundary conditions. The main contributions of this work are:

- **General boundary-aware TENG-BC Framework.** We introduce a unified boundary-aware least-squares

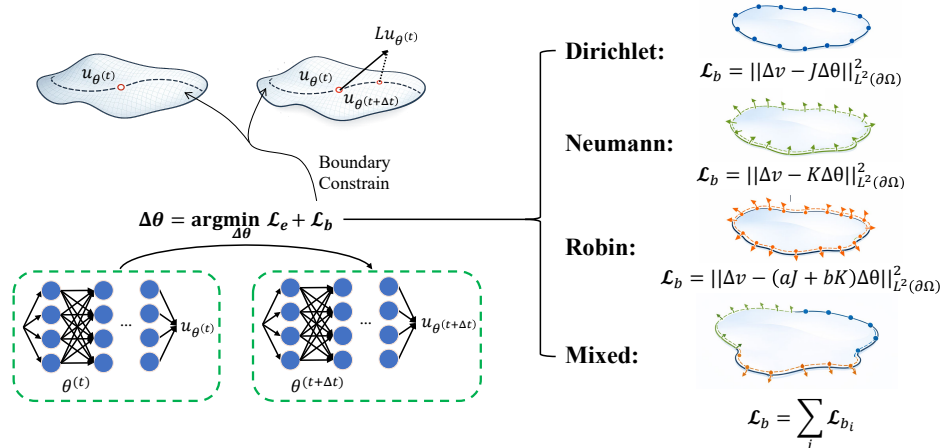


Figure 1. Overview of the boundary-aware TENG-BC update. The neural representation is advanced by solving a unified least-squares problem that enforces both interior dynamics and boundary constraints. Different boundary types are incorporated through the same optimization operator, which is repeatedly applied to realize temporal evolution.

formulation (see Figure 1) for time-evolving neural PDE solvers, enabling the consistent treatment of Dirichlet, Neumann, Robin, and mixed boundary conditions within a single optimization operator.

- **Efficient and scalable optimization.** We develop an efficient unified implementation that assembles interior and boundary constraints into a single linearized least-squares system, enabling consistent, linearly scalable updates across boundary types.
- **High accuracy performance.** We demonstrate that TENG-BC achieves stable, high-precision solutions across diffusion-dominated, advection-dominated, and nonlinear regimes, surpassing conventional solvers and PINN baselines.

2. Related Work

2.1. Neural solvers for PDEs

Neural networks have been widely adopted as function approximators for partial differential equations, enabling solution representations that are independent of predefined spatial meshes. Many existing equation-driven approaches treat time as an additional input variable and optimize the neural representation over the entire space–time domain. This strategy underlies Physics-Informed Neural Networks (PINNs) (Raissi et al., 2019; Wang & Perdikaris, 2023; Wang et al., 2021b; Sirignano & Spiliopoulos, 2018). An alternative line of work advances neural solutions through time by updating the representation sequentially. In this setting, the neural network is interpreted as a time-dependent ansatz, and evolution is realized through repeated local updates rather than global regression. Representative examples include methods derived from the time-dependent variational

principle (Dirac, 1930; Koch & Lubich, 2007; Carleo & Troyer, 2017; Du & Zaki, 2021; Berman & Peherstorfer, 2023), which project the governing dynamics onto a parameterized manifold, as well as optimization-based time integration schemes (Kochkov & Clark, 2018; Chen et al., 2023a; Gutiérrez & Mendl, 2022; Luo et al., 2022; 2023; Sinibaldi et al., 2023). Beyond equation-driven solvers, neural networks have also been employed to learn PDE dynamics directly from data. This includes operator-learning frameworks such as the Fourier Neural Operator (Li et al., 2020) and DeepONet (Lu et al., 2019). Rather than approximating a single solution trajectory, these models aim to capture mappings between function spaces and are often trained across families of PDEs.

2.2. Boundary treatment in neural PDE solvers

In neural PDE solvers, boundary constraints are typically incorporated through either soft or hard enforcement mechanisms. A widely used strategy is to impose boundary conditions through penalty terms added to the training objective. This approach is adopted by most PINN-based methods, where boundary residuals are included alongside interior PDE residuals with manually chosen weights (Raissi et al., 2019; Wang et al., 2021b). An alternative line of work seeks to enforce boundary conditions through hard constraints by construction. This is commonly achieved by modifying the neural representation to satisfy boundary conditions identically, for example through tailored trial spaces and distance functions (Lu et al., 2021; Sukumar & Srivastava, 2022). Beyond these two paradigms, several other structure-aware strategies include (Weinan et al., 2021; Liu et al., 2023) have also been explored.

3. Methods

3.1. Problem Formulation

We consider time-dependent partial differential equations (PDEs) of the form

$$u_t(x, t) = Lu(x, t), \quad x \in \Omega, \quad t \in [0, T],$$

subject to general mixed boundary conditions imposed on disjoint subsets of $\partial\Omega$,

$$[a(x)u(x, t) + b(x)\partial_n u(x, t)]|_{\partial\Omega} = v(x, t),$$

where L is a spatial differential operator and ∂_n denotes the normal derivative on the boundary. Dirichlet and Neumann conditions are recovered by setting $(a, b) = (1, 0)$ and $(0, 1)$, respectively. For Robin conditions, the coefficients $a, b \neq 0$. When representing mixed conditions, different coefficient values are taken on different segments of the boundary.

Contrast with global-in-time methods, TENG-BC represents the temporal evolution of $u(x, t)$ as a sequence of parameter-space updates on a time-dependent representation $u_{\theta^{(t)}}(x)$. Here $\theta^{(t)}$ denotes the set of parameters associated with the solution at the time step t . Rather than minimizing a global time-integrated residual, TENG-BC performs local functional optimization at each time step to update the parameters $\theta^{(t)} \rightarrow \theta^{(t+\Delta t)}$ in accordance with the governing PDE

$$\theta^{(t+\Delta t)} = \arg \min_{\theta} (\mathcal{L}_e(u_{\theta}) + \mathcal{L}_b(u_{\theta})),$$

where \mathcal{L}_e and \mathcal{L}_b denote the interior and boundary consistency terms. Specifically, $\mathcal{L}_e(u_{\theta}) := \frac{1}{2} \|u_{\theta} - u_{\text{target}}\|_{L^2(\Omega)}^2$ enforces the temporal update $u_t = Lu$, while $\mathcal{L}_b(u_{\theta}) := \frac{1}{2} \|au_{\theta} + b\partial_n u_{\theta} - v\|_{L^2(\partial\Omega)}^2$ encodes boundary constraints.

3.2. Boundary-Aware Least-Squares Stepper

Ignoring boundary effects momentarily, the update at a fixed time step is obtained by solving a local least-squares problem in parameter space. Given parameters θ , we seek an increment $\Delta\theta$ such that the first-order variation of the neural function best matches the target field u_{target} in the $L^2(\Omega)$ sense:

$$\Delta\theta_e = \arg \min_{\Delta\theta} \|\Delta u - J\Delta\theta\|_{L^2(\Omega)}^2,$$

where $J = \partial_{\theta} u_{\theta}$ and $\Delta u = u_{\text{target}} - u_{\theta}$. It has been proved in (Chen et al., 2024) that this update corresponds to the natural-gradient step (Müller & Zeinhofer, 2023) in function space, yielding a quasi-Newton update that projects the continuous PDE evolution onto the neural parameter manifold.

To incorporate boundary conditions consistently into the time-evolving optimization framework, we introduce a

boundary-aware least-squares term that accounts for value and normal-derivative constraints on $\partial\Omega$. This term complements the interior consistency objective and contributes jointly to the parameter update at each time step.

By linearizing both the neural representation u_{θ} and its normal derivative $\partial_n u_{\theta}$ with respect to the parameters, boundary conditions of the general mixed form yields the optimization problem

$$\Delta\theta_b = \arg \min_{\Delta\theta} \|\Delta v - (aJ + bK)\Delta\theta\|_{L^2(\partial\Omega)}^2, \quad (1)$$

where $J = \partial_{\theta} u_{\theta}$, $K = \partial_{\theta}(\partial_n u_{\theta})$, and $\Delta v = v - (au_{\theta} + b\partial_n u_{\theta})$ denotes the instantaneous boundary mismatch. The solution of Equation (1) represents the parameter variation required to enforce boundary consistency at the current time step. The detailed derivation of this boundary-aware least-squares formulation is provided in Section A.

The unified formulation in Equation (1) explicitly recovers standard boundary conditions as special cases by appropriate choices of (a, b, v) .

Dirichlet boundary. For Dirichlet conditions $u(x, t) = v(x, t)$ on $\partial\Omega_D$, setting $(a, b) = (1, 0)$ yields

$$\Delta\theta = \arg \min_{\Delta\theta} \|v - (u_{\theta} + J\Delta\theta)\|_{L^2(\partial\Omega_D)}^2,$$

which enforces boundary values through direct coupling between function mismatch and parameter variations.

Neumann boundary. For Neumann conditions $\partial_n u(x, t) = v(x, t)$ on $\partial\Omega_N$, choosing $(a, b) = (0, 1)$ gives

$$\Delta\theta = \arg \min_{\Delta\theta} \|v - (\partial_n u_{\theta} + K\Delta\theta)\|_{L^2(\partial\Omega_N)}^2,$$

so that normal-derivative constraints enter the optimization directly via the Jacobian K .

Robin boundary. For Robin conditions $au + b\partial_n u = v$ on $\partial\Omega_R$ with $a, b \neq 0$, the update takes the coupled form

$$\Delta\theta = \arg \min_{\Delta\theta} \|v - a(u_{\theta} + J\Delta\theta) - b(\partial_n u_{\theta} + K\Delta\theta)\|_{L^2(\partial\Omega_R)}^2,$$

where value and derivative constraints are enforced simultaneously.

Mixed boundary conditions. In the general case, the coefficients $a(x)$ and $b(x)$ may vary spatially along the boundary. Different boundary types imposed on disjoint subsets of $\partial\Omega$ therefore correspond to different values of $(a(x), b(x))$ on each boundary segment. Under this formulation, mixed boundary conditions are handled naturally by the same least-squares operator, with the corresponding terms combined additively into a single optimization problem that enforces all boundary constraints consistently at each time step.

3.3. TENG-BC: TENG with arbitrary boundaries

Combined interior–boundary update. The actual TENG-BC step at each time increment is obtained by combining interior consistency and boundary constraints within a single local least-squares problem. Specifically, the parameter update $\Delta\theta$ is computed as

$$\Delta\theta = \arg \min_{\Delta\theta} \left(\|\Delta u + J\Delta\theta\|_{L^2(\Omega)}^2 + \|\Delta v - (aJ + bK)\Delta\theta\|_{L^2(\partial\Omega)}^2 \right). \quad (2)$$

This formulation can be equivalently viewed as a unified least-squares problem over the domain closure $\bar{\Omega}$, where interior and boundary residuals are assembled under the combined $L^2(\bar{\Omega})$ inner product.

From a geometric viewpoint, this unified least-squares update also admits an interpretation as a natural-gradient step in function space. The combined $L^2(\bar{\Omega})$ norm induces a metric that couples interior variations and boundary variations through the Jacobian terms J and K . Under this metric, the solution of the least-squares problem corresponds to the steepest descent direction in function space projected onto the parameter manifold. A detailed derivation and analysis are provided in Section B.

Its practical implementation at each time step is summarized in Algorithm 1. At each update, the parameter increment is obtained by explicitly assembling an augmented design matrix \mathcal{J} that stacks interior and boundary Jacobian blocks, and solving the resulting linearized least-squares system, rather than backpropagating through the full boundary loss. Because the Jacobian contributions from interior samples and boundary samples are combined into one unified matrix, all boundary types are handled within the same computational pipeline without introducing specialized branches. As a result, the per-step computational cost scales linearly with the number of sampled interior and boundary points.

Compared with common boundary-handling strategies in neural PDE solvers, this formulation embeds boundary information directly into the optimization operator itself. Unlike approaches that explicitly construct boundary-satisfying trial spaces, the proposed method does not restrict the functional representation and therefore remains applicable to complex mixed or time-dependent boundary constraints. In contrast to penalty-based formulations, boundary constraints are not enforced through additional loss terms or heuristic weighting, but are integrated into the same least-squares geometry as the interior dynamics. As a result, boundary conditions are forced with high accuracy during the optimization trajectory at each time step. This intrinsic enforcement preserves correct boundary evolution and promotes stable, physically meaningful convergence throughout the time-marching process.

Algorithm 1 Boundary-Aware TENG Update at One Time Step

- 1: **Input:** Current parameters $\theta^{(t)}$, target field u_{target} , boundary data (a, b, v)
- 2: **Output:** Updated parameters $\theta^{(t+\Delta t)}$
- 3: Initialize $\theta \leftarrow \theta^{(t)}$
- 4: **for** $k = 1$ to N_{LS} **do**
- 5: Compute interior residual $\Delta u = u_{\text{target}} - u_\theta$ on Ω
- 6: Compute boundary mismatch $\Delta v = v - (au_\theta + b\partial_n u_\theta)$ on $\partial\Omega$
- 7: Compute interior Jacobian $J_\Omega = \partial_\theta u_\theta$ on Ω
- 8: Compute boundary Jacobians $J_{\partial\Omega} = \partial_\theta u_\theta$, $K_{\partial\Omega} = \partial_\theta(\partial_n u_\theta)$ on $\partial\Omega$
- 9: Form the unified residual $\mathcal{R} = (\Delta u, \Delta v)$
- 10: Form the unified Jacobian $\mathcal{J} = (J_\Omega, aJ_{\partial\Omega} + bK_{\partial\Omega})$
- 11: Solve the unified least-squares problem

$$\Delta\theta \leftarrow \arg \min_{\Delta\theta} \|\mathcal{R} - \mathcal{J}\Delta\theta\|_{L^2(\bar{\Omega})}^2$$

- 12: Update parameters $\theta \leftarrow \theta + \Delta\theta$
 - 13: **end for**
 - 14: Set $\theta^{(t+\Delta t)} \leftarrow \theta$
-

Temporal discretization. Different time integration schemes correspond to different constructions of the target function u_{target} . In the simplest case, the **TENG–Euler** scheme uses

$$u_{\text{target}} = u_{\theta^{(t)}} + \Delta t L(u_{\theta^{(t)}}).$$

Higher-order schemes, such as **TENG–Heun** and **TENG–RK4** (see detailed time evolving schemes in Section C), introduce multiple intermediate evaluations of the operator $L(\cdot)$ to form more accurate targets, while keeping the same optimization mechanism at each substage. Importantly, the least-squares stepper used to fit each target remains identical across different integration orders.

3.4. Implementation Details

The practical implementation of TENG-BC involves several design considerations that ensure stable and accurate optimization in high-dimensional neural representations. While the underlying formulation is continuous in both space and time, numerical realization requires discrete sampling, stable least-squares solvers, and efficient parameter updates.

(i) *Spatial Sampling and Discrete Least-Squares Approximation.* We employ discrete spatial sampling to approximate the continuous functional optimization. At each time step, a finite set of interior points $\{x_i\}_{i=1}^{N_\Omega}$ is drawn from the domain Ω , and boundary samples $\{x_j\}_{j=1}^{N_{\partial\Omega}}$ are collected from $\partial\Omega$. For every sampled point, the corresponding Jacobian quantities $J = \partial_\theta u_\theta(x_i)$ and $K = \partial_\theta(\partial_n u_\theta)(x_j)$ are

computed through automatic differentiation, forming finite matrices that approximate the continuous functional operators. The least-squares system is then solved empirically under this discrete setting, effectively replacing the L^2 inner product by Monte Carlo quadrature.

(ii) *Temporal Consistency in Boundary Enforcement.* When boundary conditions vary in time, the boundary-aware least-squares stepper enforces constraints corresponding to the correct temporal stage of each substep. For instance, in the RK4 integration scheme, intermediate targets evaluated at $t + \Delta t/2$ use boundary values $v(x, t + \Delta t/2)$, while the final target at $t + \Delta t$ enforces $v(x, t + \Delta t)$. This temporal alignment ensures that every optimization remains consistent with the instantaneous boundary condition, preserving both physical fidelity and numerical stability across multi-stage propagation.

(iii) *Numerical Stabilization and Singular-Value Truncation.* To maintain numerical stability during least-squares refinement, small singular values in the local Jacobian matrices are truncated, preventing ill-conditioned updates and filtering noisy gradient directions. All computations are performed in double precision, which further mitigates accumulation of round-off errors over successive iterations. These stabilization measures ensure that each least-squares solution remains well-conditioned even when the local parameter geometry exhibits strong anisotropy.

(iv) *Partial Parameter Updates for Stable Optimization.* Given the over-parameterized nature of neural networks, only a subset of parameters is updated during each least-squares iteration, while the remaining weights are temporarily fixed. This partial-update strategy reduces the dimensionality of the local system and improves conditioning without compromising representational power. Empirically, it yields smoother convergence and prevents oscillatory behavior that can arise when all parameters are jointly optimized at every step.

Together, these implementation strategies ensure that the TENG-BC framework achieves both stability and precision across diverse PDE systems. They bridge the gap between the continuous functional formulation and its discrete neural realization, enabling robust training dynamics and high-fidelity solution accuracy in all experiments presented below.

4. Results

4.1. Experimental Setup

To evaluate the capability and robustness of TENG-BC, we conduct a series of benchmark experiments spanning representative types of PDE dynamics. These include diffusion-dominated (*heat equation*), advection-dominated (*transport*

equation), and nonlinear coupled regimes (*viscous Burgers equation*), each designed to highlight distinct numerical and physical challenges such as stability, sharp-front preservation, and multiple boundary conditions.

In all cases, the neural representation $u_{\theta(t)}(x)$ is modeled by a fully connected network (see Section C) whose parameters are updated through the TENG-BC algorithm described above. The network takes the spatial coordinates $x \in \Omega \subset \mathbb{R}^d$ as input and outputs a scalar field value. All experiments share a common optimization pipeline to ensure cross-equation comparability. In all experiments, TENG-BC advances the solution using a fixed time step size $\Delta t = 5 \times 10^{-4}$.

For comparison, we include a standard Physics-Informed Neural Network (PINN) trained with BFGS or ENG optimizer (Müller & Zeinhofer, 2023) and a finite-element-method (FEM) baseline (Gustafsson & McBain, 2020) using the same number of spatial sampling points. Each equation is solved by TENG-BC with identical network architecture and comparable sampling density to ensure fairness across tasks. Further implementation details (data sampling strategy, numerical precision, and optimization hyperparameters) are provided in Section C, together with the full specifications of each PDE system, including initial and boundary conditions, baseline solver configurations, and all parameter settings for reproducibility.

4.2. Heat Equation with Different Boundaries

We first evaluate the proposed TENG-BC framework on the two-dimensional heat equation,

$$u_t = \kappa \nabla^2 u$$

to examine its capability of handling different boundary formulations. Four boundary types are considered: Dirichlet, Neumann, Mixed, and Robin. For the Neumann case, both zero and nonzero flux conditions are tested to assess sensitivity to boundary value. All simulations are conducted on the circular domain $\{r \leq 1\}$, except for the mixed-boundary condition, which is computed on a quarter-annulus region $\{0.5 \leq r \leq 1, 0 \leq \theta \leq \frac{\pi}{2}\}$. For quantitative evaluation, the analytic solution is used as the reference field.

Figure 2 summarizes the quantitative performance of TENG-BC, illustrating how different algorithmic variants behave under identical experimental settings. To assess the influence of temporal propagation on overall accuracy, we test three time discretization schemes of different formal orders. As shown in Table 1, both TENG-Heun and TENG-RK4 achieve comparable accuracy and significantly outperform the first-order TENG-Euler across most boundary conditions, consistent with their reduced local truncation error. The Heun variant offers an attractive balance between precision and computational efficiency, reaching nearly the same

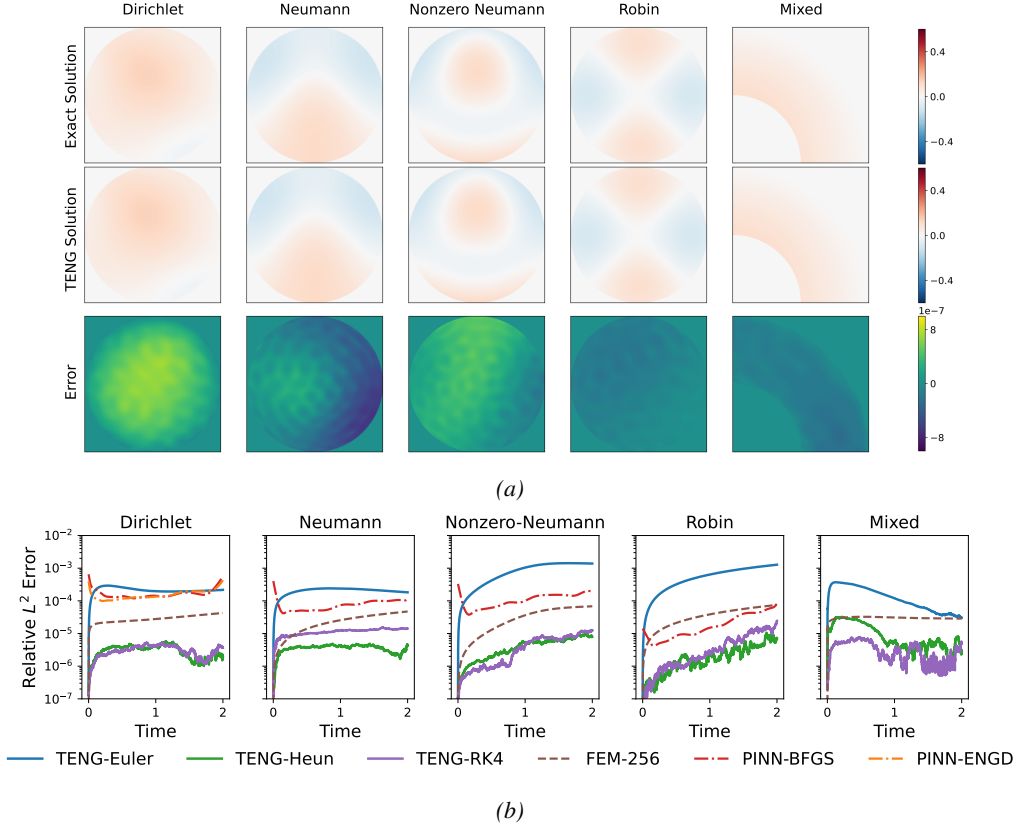


Figure 2. Performance of TENG-BC on heat equation with different boundary conditions. (a) TENG-Heun predictions at $T = 1.0$ are shown with analytic references and pointwise error maps. (b) Per-time-step relative L^2 -error comparison among TENG-BC variants and other reference solvers.

accuracy as RK4 while requiring roughly half the training cost.

Figure 2a visualizes the predicted solutions by TENG-Heun and their deviations from the analytic reference at $T = 1.0$. Across all types of boundaries, TENG-BC captures both the steady decay patterns and fine-scale diffusion features with negligible deviation from the exact profile. The accumulated spatial error remains at the 10^{-7} level, confirming that the per-step least-squares fitting effectively preserves both physical smoothness and long-term stability. In the mixed-boundary condition, where distinct constraint types coexist on different parts of the domain, the network maintains excellent continuity across the transition interface—demonstrating the effectiveness of the unified boundary treatment. Overall, these visual results highlight TENG-BC’s capability to produce high-fidelity continuous solutions under diverse boundary conditions within a single training framework.

Figure 2b includes the per-time-step relative L^2 -error comparison among TENG-BC variants and reference solvers, including PINN and the finite-element method (FEM). Across the entire evolution range, TENG-Heun and TENG-RK4

models maintain markedly lower relative error and exhibit smoother temporal variation than the baseline methods. The PINN curves show relatively large errors throughout the entire time span, revealing its difficulty in accurately convergence and capturing temporal dependencies. The FEM solutions start with smaller initial errors due to its mesh-based representation of the initial condition but deteriorate rapidly over time as discretization and interpolation errors accumulate. In contrast, TENG-BC sustains uniformly low relative error throughout training, with minimal drift over long horizons, demonstrating that its optimization effectively suppresses cumulative numerical error and preserves temporal consistency of the learned solution.

4.3. Transport Equation on Circular Domain

We further evaluate TENG-BC on the two-dimensional transport equation

$$\partial_t u + v(x) \cdot \nabla u = 0$$

which governs purely advective dynamics. Unlike the heat equation, where diffusion naturally damps perturbations and dissipates error, the transport equation propagates information along characteristic directions, causing any local

Table 1. Full-time-range relative L^2 -error of TENG-BC with three propagation schemes on heat equation with different boundary conditions.

| L^2 -error↓ | Dirichlet | Neumann | Nonzero Neumann | Robin | Mixed |
|---------------|-----------------|-----------------|-----------------|-----------------|-----------------|
| TENG-Euler | 2.17e-04 | 2.05e-04 | 9.04e-04 | 6.40e-04 | 1.25e-04 |
| TENG-Heun | 3.08e-06 | 3.60e-06 | 4.41e-06 | 2.42e-06 | 1.15e-05 |
| TENG-RK4 | 3.07e-06 | 1.14e-05 | 4.72e-06 | 5.00e-06 | 3.31e-06 |

mismatch to persist and gradually accumulate over time. This setting therefore provides a stringent test of numerical stability and accuracy for function-based solvers.

The simulation is performed on a circular domain $\{r \leq 1\}$ with inhomogeneous Dirichlet boundary, prescribing a spatially varying inflow profile that continuously injects information. This configuration prevents convergence to a trivial steady state and emphasizes the model’s ability to represent non-equilibrium transport processes. The analytic reference is constructed by tracing the initial and boundary conditions along characteristic trajectories.

As reported in Figure 3, the growth of relative error remains bounded and physically consistent with the underlying hyperbolic dynamics. The predicted solution therefore maintains consistent accuracy over time, with mean-squared errors uniformly lower than those of PINN and FEM baselines. Notably, this level of accuracy is achieved despite the absence of dissipative mechanisms, under which error growth is typically expected.

4.4. Burgers Equation with periodic boundary

We finally evaluate TENG-BC on the two-dimensional viscous Burgers equation,

$$u_t + u(\partial_{x_1} u + \partial_{x_2} u) = \nu \nabla^2 u,$$

with a small diffusion coefficient $\nu = 10^{-3}$. This configuration produces highly nonlinear dynamics with sharp gradients and near-discontinuous transitions in the solution profile, a regime notoriously difficult for both neural and conventional numerical solvers. Since the viscous Burgers equation lacks a closed-form analytic solution, a spectral solver (Canuto et al., 2007) with 1024 modes is employed as the reference field.

In our experiment, TENG-BC accurately reconstructs the nonlinear propagation and sharp front formation throughout the evolution on a square domain $[0, 2\pi]^2$ with periodic boundaries in both directions. As illustrated in Figure 4a, the predicted fields by TENG-Heun remain sharply resolved yet physically smooth, showing no spurious oscillations or excessive numerical diffusion even near the discontinuity. Residual errors are tightly localized along the shock front, while the remaining regions maintain near-perfect agreement with the spectral reference.

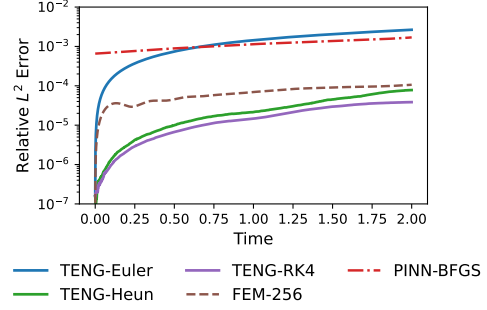


Figure 3. Performance of TENG-BC on the two-dimensional transport equation with nonzero Dirichlet boundary. Comparison of per-time-step relative L^2 -error among TENG-BC variants, PINN, and FEM baselines.

Figure 4b, Figure 4c and Figure 4d demonstrates the superior performance of TENG-BC over FEM for Burgers equation with periodic boundary. Figure 4b quantifies the difference between TENG-Heun and finite-element (FEM) solutions across multiple spatial resolutions. The plotted quantity represents the L^2 norm of the discrepancy between TENG-BC and FEM results, $\|u_{\text{FEM}} - u_{\text{TENG}}\|_2$, evaluated at successive time steps. As the FEM resolution increases, this difference decreases monotonically, indicating that FEM progressively converges toward the TENG-BC solution rather than the reverse. Figure 4c further illustrates the error scaling at $T = 4$ with respect to FEM resolution, which exhibits a smooth and nearly linear decrease in the log-log scale. This trend persists up to the FEM-256 configuration, beyond which further refinement produces diminishing improvements, suggesting that TENG-BC’s continuous functional representation achieves an accuracy exceeding that of the high-resolution FEM and closely approaches the reference limit.

As the Burgers dynamics evolve, the three solvers begin to diverge in distinct ways, which further demonstrate this conclusion. Pairwise comparisons among TENG-Heun, FEM-256, and spectral-1024 in Figure 4d reveal that the FEM-related differences rise abruptly around $T \approx 1.5$, coinciding with the emergence of the steep shock. At this stage, the FEM-related differences (FEM-TENG and FEM-Spectral) rise abruptly, indicating that the finite-element solver begins to lose consistency earlier than the other methods as the gradient intensifies. In contrast, the TENG-Spectral curve

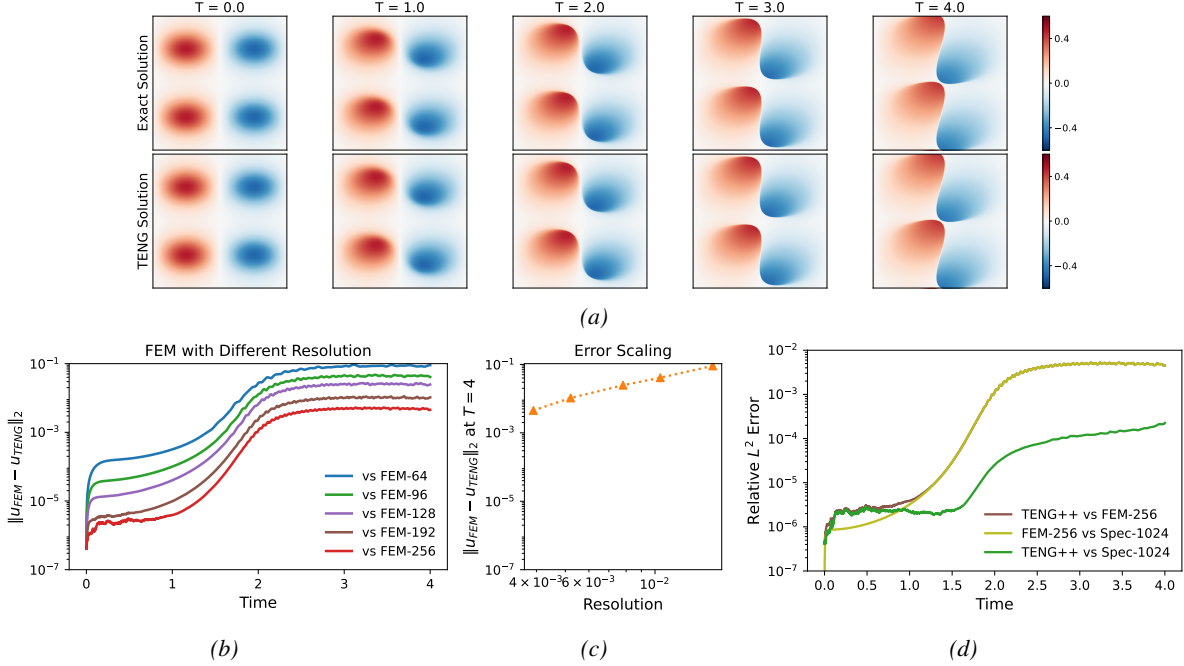


Figure 4. Performance of TENG-BC on the Burgers equation with periodic boundary. (a) Predicted solutions by TENG-Heun at representative time steps. (b) Discrepancies between TENG-Heun and FEM solutions across multiple spatial resolutions (c) the scaling trend of discrepancies. between TENG-Heun and FEM solutions at $T = 4$. (d) Pairwise L^2 discrepancies among TENG-Heun, FEM-256, and spectral-1024 solvers.

Table 2. Relative L^2 errors of different solvers for the Burgers equation with periodic boundary conditions, measured against the spectral-1024 reference.

| L^2 -error \downarrow | $T = 1$ | $T = 2$ | $T = 3$ | $T = 4$ |
|---------------------------|-----------------|-----------------|-----------------|-----------------|
| TENG-Euler | 2.97e-04 | 1.72e-03 | 1.28e-03 | 1.60e-03 |
| TENG-Heun | 2.24e-06 | 2.52e-05 | 1.15e-04 | 2.24e-04 |
| TENG-RK4 | 2.63e-06 | 2.94e-05 | 1.42e-04 | 3.21e-04 |
| FEM | 3.21e-06 | 1.11e-03 | 4.83e-03 | 4.50e-03 |
| PINN-BFGS | 1.28e-01 | 1.99e-01 | 2.08e-01 | 1.71e-01 |

exhibits a much milder and delayed increase, implying that both methods continue to represent the evolving front coherently until substantially stronger nonlinearities develop.

A quantitative comparison against the spectral-1024 reference is summarized in Table 2. TENG-BC consistently achieves the smallest deviation from the spectral solution across all recorded times, maintaining 10^{-4} accuracy even as nonlinear gradients intensify. In contrast, FEM errors increase of magnitude 10^3 after the onset of the shock, and PINN exhibits uniformly larger discrepancies throughout the simulation.

Together, these results highlight TENG-BC’s robustness: while all solvers encounter growing numerical challenges near the shock, TENG-BC maintains stable optimization

and consistent solution quality well beyond the point where traditional solver begins to fail.

5. Discussion

A central contribution of the TENG-BC framework lies in its treatment of boundary conditions within time-dependent neural PDE solvers. Rather than enforcing boundaries through penalty terms or problem-specific trial-space constructions, TENG-BC incorporates boundary constraints directly into the same local optimization operator that governs interior evolution. This formulation enables Dirichlet, Neumann, Robin, and mixed boundary conditions to be enforced intrinsically at every time step, providing a unified mechanism that remains applicable across heterogeneous and time-dependent boundary constraints.

This intrinsic enforcement avoids sensitivity to loss weighting and preserves coherent boundary evolution even in long-time simulations, leading to solver-level accuracy that consistently matches or outperforms classical discretization-based solvers and PINN baselines. These results suggest that treating boundary conditions as first-class components of the optimization operator, rather than auxiliary constraints, is essential for reliable neural PDE integration and provides a foundation for future extensions to Cauchy-type and more general boundary value problems.

Acknowledgements

We gratefully acknowledge Zhuo Chen for many insightful and valuable discussions that greatly benefited the project. This work is partially supported by the elite undergraduate training program of the School of Mathematical Sciences at Peking University.

Impact Statement

This work contributes to the development of reliable neural solvers for time-dependent partial differential equations with general boundary conditions. By demonstrating that high accuracy and stability can be achieved through localized, equation-consistent optimization, it provides a principled alternative to global-in-time training strategies commonly used in scientific machine learning. The proposed framework has potential impact across scientific and engineering domains where accurate long-time simulation and complex boundary handling are essential, such as fluid dynamics, transport phenomena, and multi-physics modeling. More broadly, it suggests that neural methods need not trade precision for flexibility, and that grounding learning dynamics in the structure of governing equations can improve both robustness and general applicability. The ideas presented here may also inform future developments in stochastic, parametric, and coupled systems, as well as hybrid approaches that combine data-driven models with physically constrained time evolution.

References

Berman, J. and Peherstorfer, B. Randomized sparse neural galerkin schemes for solving evolution equations with deep networks. In *Thirty-seventh Conference on Neural Information Processing Systems*, 2023.

Canuto, C., Hussaini, M. Y., Quarteroni, A., and Zang, T. A. *Spectral methods: evolution to complex geometries and applications to fluid dynamics*. Springer Science & Business Media, 2007.

Carleo, G. and Troyer, M. Solving the quantum many-body problem with artificial neural networks. *Science*, 355 (6325):602–606, 2017.

Chen, H., Wu, R., Grinspun, E., Zheng, C., and Chen, P. Y. Implicit neural spatial representations for time-dependent pdes. In *International Conference on Machine Learning*, pp. 5162–5177. PMLR, 2023a.

Chen, Z., Luo, D., Hu, K., and Clark, B. K. Simulating 2+1d lattice quantum electrodynamics at finite density with neural flow wavefunctions. *arXiv preprint arXiv:2212.06835*, 2022.

Chen, Z., Newhouse, L., Chen, E., Luo, D., and Soljagic, M. Antn: Bridging autoregressive neural networks and tensor networks for quantum many-body simulation. In Oh, A., Neumann, T., Globerson, A., Saenko, K., Hardt, M., and Levine, S. (eds.), *Advances in Neural Information Processing Systems*, volume 36, pp. 450–476. Curran Associates, Inc., 2023b.

Chen, Z., McCarran, J., Vizcaino, E., Soljagic, M., and Luo, D. TENG: Time-evolving natural gradient for solving PDEs with deep neural nets toward machine precision. In *Forty-first International Conference on Machine Learning*, 2024. URL <https://openreview.net/forum?id=v1I4zRAjMb>.

Dirac, P. A. Note on exchange phenomena in the thomas atom. In *Mathematical proceedings of the Cambridge philosophical society*, volume 26, pp. 376–385. Cambridge University Press, 1930.

Du, Y. and Zaki, T. A. Evolutional deep neural network. *Physical Review E*, 104(4), October 2021. ISSN 2470-0053. doi: 10.1103/physreve.104.045303.

Gustafsson, T. and McBain, G. D. scikit-fem: A Python package for finite element assembly. *Journal of Open Source Software*, 5(52):2369, 2020. doi: 10.21105/joss.02369.

Gutiérrez, I. L. and Mendl, C. B. Real time evolution with neural-network quantum states. *Quantum*, 6:627, 2022.

Han, J., Jentzen, A., et al. Deep learning-based numerical methods for high-dimensional parabolic partial differential equations and backward stochastic differential equations. *Communications in mathematics and statistics*, 5 (4):349–380, 2017.

Koch, O. and Lubich, C. Dynamical low-rank approximation. *SIAM Journal on Matrix Analysis and Applications*, 29(2):434–454, 2007.

Kochkov, D. and Clark, B. K. Variational optimization in the ai era: Computational graph states and supervised wavefunction optimization. *arXiv preprint arXiv:1811.12423*, 2018.

Krishnapriyan, A. S., Gholami, A., Zhe, S., Kirby, R., and Mahoney, M. W. Characterizing possible failure modes in physics-informed neural networks. *Advances in Neural Information Processing Systems*, 34, 2021.

Langley, P. Crafting papers on machine learning. In Langley, P. (ed.), *Proceedings of the 17th International Conference on Machine Learning (ICML 2000)*, pp. 1207–1216, Stanford, CA, 2000. Morgan Kaufmann.

- Li, Z., Kovachki, N., Azizzadenesheli, K., Liu, B., Bhattacharya, K., Stuart, A., and Anandkumar, A. Fourier neural operator for parametric partial differential equations. *arXiv preprint arXiv:2010.08895*, 2020.
- Liu, N., Jafarzadeh, S., and Yu, Y. Domain agnostic fourier neural operators, 2023. URL <https://arxiv.org/abs/2305.00478>.
- Long, Z., Lu, Y., Ma, X., and Dong, B. Pde-net: Learning pdes from data. In *International conference on machine learning*, pp. 3208–3216. PMLR, 2018.
- Lu, L., Jin, P., and Karniadakis, G. E. Deeponet: Learning nonlinear operators for identifying differential equations based on the universal approximation theorem of operators. *arXiv preprint arXiv:1910.03193*, 2019.
- Lu, L., Pestourie, R., Yao, W., Wang, Z., Verdugo, F., and Johnson, S. G. Physics-informed neural networks with hard constraints for inverse design. *SIAM Journal on Scientific Computing*, 43(6):B1105–B1132, 2021. doi: 10.1137/21M1397908.
- Luo, D., Chen, Z., Carrasquilla, J., and Clark, B. K. Autoregressive neural network for simulating open quantum systems via a probabilistic formulation. *Physical review letters*, 128(9):090501, 2022.
- Luo, D., Chen, Z., Hu, K., Zhao, Z., Hur, V. M., and Clark, B. K. Gauge-invariant and anyonic-symmetric autoregressive neural network for quantum lattice models. *Physical Review Research*, 5(1):013216, 2023.
- Müller, J. and Zeinhofer, M. Achieving high accuracy with pinns via energy natural gradient descent. In *International Conference on Machine Learning*, pp. 25471–25485. PMLR, 2023.
- Raissi, M., Perdikaris, P., and Karniadakis, G. E. Physics-informed neural networks: A deep learning framework for solving forward and inverse problems involving nonlinear partial differential equations. *Journal of Computational physics*, 378:686–707, 2019.
- Sinibaldi, A., Giuliani, C., Carleo, G., and Vicentini, F. Unbiasing time-dependent Variational Monte Carlo by projected quantum evolution. *Quantum*, 7:1131, October 2023. ISSN 2521-327X. doi: 10.22331/q-2023-10-10-1131.
- Sirignano, J. and Spiliopoulos, K. Dgm: A deep learning algorithm for solving partial differential equations. *Journal of computational physics*, 375:1339–1364, 2018.
- Sukumar, N. and Srivastava, A. Exact imposition of boundary conditions with distance functions in physics-informed deep neural networks. *Computer Methods in Applied Mechanics and Engineering*, 389:114333, February 2022. ISSN 0045-7825. doi: 10.1016/j.cma.2021.114333. URL <http://dx.doi.org/10.1016/j.cma.2021.114333>.
- Wang, J., Chen, Z., Luo, D., Zhao, Z., Hur, V. M., and Clark, B. K. Spacetime neural network for high dimensional quantum dynamics. *arXiv preprint arXiv:2108.02200*, 2021a.
- Wang, S. and Perdikaris, P. Long-time integration of parametric evolution equations with physics-informed deep-onets. *Journal of Computational Physics*, 475:111855, 2023.
- Wang, S., Wang, H., and Perdikaris, P. Learning the solution operator of parametric partial differential equations with physics-informed deep-onets. *Science advances*, 7(40): eabi8605, 2021b.
- Wang, S., Sankaran, S., and Perdikaris, P. Respecting causality for training physics-informed neural networks. *Computer Methods in Applied Mechanics and Engineering*, 421:116813, 2024.
- Weinan, E., Han, J., and Jentzen, A. Algorithms for solving high dimensional pdes: from nonlinear monte carlo to machine learning. *Nonlinearity*, 35(1):278, 2021.
- Yu, B. et al. The deep ritz method: a deep learning-based numerical algorithm for solving variational problems. *Communications in Mathematics and Statistics*, 6(1):1–12, 2018.

A. Derivation of the Boundary-Aware Least-Squares Formulation

For completeness, we include the derivation of the boundary-aware least-squares stepper that was omitted from the main text. Starting from the boundary functional

$$\mathcal{L}_b(u_\theta) = \frac{1}{2} \|au_\theta + b\partial_n u_\theta - v\|_{L^2(\partial\Omega)}^2,$$

each boundary condition enters the optimization through its own contribution. Here, the existence of $\partial_n u_\theta$ makes the direct extension from simply fitting the target function to the boundary-constrained case non-trivial. We treat u_θ and $\partial_n u_\theta$ as jointly parameterized quantities. The least-squares update that minimizes \mathcal{L}_b then takes the form

$$\begin{aligned} \Delta\theta = \arg \min_{\Delta\theta} & \left\| (v - au_\theta - b\partial_n u_\theta)(\cdot) - a(\cdot) \sum_j \frac{\partial u_\theta}{\partial \theta_j}(\cdot) \Delta\theta_j \right. \\ & \left. - b(\cdot) \sum_k \frac{\partial(\partial_n u_\theta)}{\partial \theta_k}(\cdot) \Delta\theta_k \right\|_{L^2(\partial\Omega)}^2. \end{aligned}$$

This can be compactly written as

$$\Delta\theta = \arg \min_{\Delta\theta} \|\Delta v - (aJ + bK)\Delta\theta\|_{L^2(\partial\Omega)}^2,$$

where J , K and Δv are defined as in Equation (1).

When $(a, b, v) = (1, 0, u_{\text{target}})$, the boundary-consistency term becomes identical to the interior consistency objective. In this case, the interior and boundary contributions share the same residual structure and can be written in a unified form over the domain closure $\bar{\Omega}$:

$$\Delta\theta = \arg \min_{\Delta\theta} \|\Delta v - (aJ + bK)\Delta\theta\|_{L^2(\bar{\Omega})}^2, \quad (3)$$

which is equivalent to the combined interior–boundary formulation in Equation (2) from the main text. The function norm $L^2(\bar{\Omega})$ denotes the combined interior–boundary L^2 norm, incorporating both \int_Ω and $\int_{\partial\Omega}$ contributions. This expression defines the boundary-aware least-squares stepper used throughout the algorithm.

B. Theoretical Interpret as Natural Gradient

We show that the TENG-BC stepper can be viewed as a natural-gradient flow in parameter space. Starting with the simple case where the boundary loss is not included, the temporal evolution of the PDE solution satisfies $u_t = Lu$, and the natural-gradient flow seeks a parameter update $\Delta\theta$ such that the induced function variation $\delta u = J(\theta)\Delta\theta$ best approximates this evolution in the L^2 sense:

$$\begin{aligned} \Delta\theta &= \arg \min_{\Delta\theta} \|(u_{\text{target}} - u_\theta) - J(\theta)\Delta\theta\|_{L^2(\Omega)}^2 \\ &= \arg \min_{\Delta\theta} \left\| -\frac{\partial \mathcal{L}_e}{\partial u_\theta} - J(\theta)\Delta\theta \right\|_{L^2(\Omega)}^2 \end{aligned}$$

whose normal equation gives

$$\begin{aligned} G(\theta)\Delta\theta &= -\int_\Omega J^T \frac{\partial \mathcal{L}_e}{\partial u_\theta} dx = -\nabla_\theta \mathcal{L}_e, \\ G(\theta) &= \int_\Omega J^T J dx. \end{aligned}$$

This leads to the standard natural-gradient update

$$\Delta\theta = -G(\theta)^{-1} \nabla_\theta \mathcal{L}_e(u_\theta), \quad (4)$$

where the metric tensor $G(\theta)$ takes the same form as the Hilbert gram matrix from (Müller & Zeinhofer, 2023), which defines the Riemannian geometry of the parameter manifold induced by the L^2 inner product in function space.

When boundary constraints are included, the update of θ can be described by Equation (3). For simplicity, we write the total loss $\mathcal{L} = \mathcal{L}_e + \mathcal{L}_b$ in the unified form of:

$$\mathcal{L} = \frac{1}{2} \|au_\theta + b\partial_n u_\theta - v\|_{L^2(\bar{\Omega})}^2.$$

It is easy to check that when $(a, b, v) = (1, 0, u_{\text{target}})$, the interior integral term reduces to the interior residual. Noticing that $\frac{\partial \mathcal{L}}{\partial u_\theta} = -a\Delta v$ and $\frac{\partial \mathcal{L}}{\partial(\partial_n u_\theta)} = -b\Delta v$, the corresponding normal equation of Equation (3) gives:

$$\begin{aligned} G(\theta)\Delta\theta &= \int_{\bar{\Omega}} (aJ + bK)^T \Delta v \, dx = - \int_{\bar{\Omega}} J^T \frac{\partial \mathcal{L}}{\partial u_\theta} \, dx - \int_{\bar{\Omega}} K^T \frac{\partial \mathcal{L}}{\partial(\partial_n u_\theta)} \, dx = -\nabla_\theta \mathcal{L}, \\ G(\theta) &= \int_{\bar{\Omega}} (aJ + bK)^T (aJ + bK) \, dx. \end{aligned}$$

Therefore the same formulation in Equation (4) extends naturally to the closure $\bar{\Omega}$ by augmenting the metric as

$$G(\theta) = \int_{\Omega} J^T J \, dx + \int_{\partial\Omega} (aJ + bK)^T (aJ + bK) \, dx, \quad (5)$$

ensuring that both interior dynamics and boundary evolution are geometrically consistent within the same optimization operator. This expression shows that the inclusion of boundary terms simply extends the inner product that defines the Riemannian metric on the parameter manifold—from one defined purely over Ω to one over the closure $\bar{\Omega}$ that couples interior and boundary contributions.

Therefore, the boundary-aware least-squares stepper can be interpreted as a realization of a natural-gradient update with the parameter metric defined in Equation (5). This establishes the formal equivalence between the TENG-BC stepper and the natural-gradient flow, even in the presence of mixed boundary conditions.

C. Experimental Settings

C.1. Neural Network Architectures and Optimization Details

Network architecture. Specifically, we adopt a multilayer perceptron (MLP) with 7 hidden layers and width 40 per layer, using activation function $\tanh(\cdot)$ to ensure sufficient regularity of the neural representation. The network parameters at time step t are denoted by $\theta^{(t)}$, and the temporal evolution of the solution is realized through a sequence of parameter updates $\theta^{(t)} \rightarrow \theta^{(t+1)}$, rather than by introducing time as an explicit input variable.

For the Burgers equation defined on the periodic domain $[0, 2\pi]^2$, we enforce periodic boundary conditions through a periodic embedding applied to the spatial inputs. The periodic embedding function is defined as:

$$\text{embedding}(x) = \text{concatenate} [a_j \cos(x_1 + \phi_j) + c_j, a_j \cos(x_2 + \phi_j) + c_j],$$

where a, ϕ and c are all trainable variables. The embedding size of each x_i ($i = 1, 2$) is 20. This embedding ensures that the neural representation is exactly periodic by construction, eliminating the need for explicit boundary constraints or penalty terms. The remaining network architectures are identical to those used in non-periodic settings, and the periodic embedding is only applied to experiments with periodic boundary conditions.

Sampling. In all experiments, the collocation points used for the local optimization are fixed across time steps and are placed on a uniform grid over the spatial domain. Both interior and boundary points remain identical throughout the temporal evolution, and no resampling is performed between successive optimization steps. We empirically observe that alternative sampling strategies, including resampling at each time step or using randomly distributed points, do not lead to noticeable differences in the final solution accuracy or convergence behavior. Therefore, a fixed grid-based sampling strategy is adopted for simplicity and reproducibility.

Time evolving schemes We use the same time evolving schemes as in (Chen et al., 2024). The update of Heun scheme can be write as:

$$\begin{aligned} k_1 &= Lu^{(t)} \\ u^{(t+1/2\Delta t)} &= u^{(t)} + k_1\Delta t \\ k_2 &= Lu^{(t+1/2\Delta t)} \\ u_{\text{target}} &= u^{(t)} + \frac{1}{2}(k_1 + k_2)\Delta t. \end{aligned}$$

The update of RK4 scheme can be write as:

$$\begin{aligned} k_1 &= Lu^{(t)} \\ u^{(t+1/4\Delta t)} &= u^{(t)} + \frac{1}{2}k_1\Delta t \\ k_2 &= Lu^{(t+1/4\Delta t)} \\ u^{(t+1/2\Delta t)} &= u^{(t)} + \frac{1}{2}k_2\Delta t \\ k_3 &= Lu^{(t+1/2\Delta t)} \\ u^{(t+3/4\Delta t)} &= u^{(t)} + k_3\Delta t \\ k_4 &= Lu^{(t+3/4\Delta t)} \\ u_{\text{target}} &= u^{(t)} + \frac{1}{6}(k_1 + 2k_2 + 2k_3 + k_4)\Delta t. \end{aligned}$$

Optimization hyperparameters. At each time step, the local least-squares problem is solved using a fixed number of optimization iterations. Unless otherwise specified, we perform 5 optimization steps per time level. To control computational cost and improve numerical stability, at each time step, 512 parameters are allowed to vary, while the remaining parameters are held fixed. The subset of active parameters is randomly chosen at each optimization step.

For multi-stage time discretization schemes such as Heun’s method and the fourth-order Runge–Kutta (RK4) method, the first stage involves a more accurate initialization of the intermediate target. Accordingly, we perform 7 optimization steps for the first target in these schemes and allow a larger active parameter subset of size 768 at the first optimization step, while all subsequent stages follow the standard setting described above. This strategy was found to provide stable and consistent convergence across all experiments.

Computational environment and other implementation details. All experiments are conducted on a single NVIDIA V100 GPU with 16GB memory. Double-precision arithmetic is used throughout to ensure numerical stability. The same random seed is used across different methods for data sampling and parameter initialization to ensure reproducibility.

C.2. Heat Equation

We consider a collection of heat equation experiments with different boundary condition configurations. All experiments solve the heat equation

$$\partial_t u(x, t) = \kappa \Delta u(x, t), \quad x \in \Omega \subset \mathbb{R}^2$$

where $\kappa = 0.1$ is the diffusion coefficient. Let (r, θ) be the polar coordinates. All simulations are conducted on the circular domain $\Omega = \{r \leq 1\}$, except for the mixed-boundary configuration, which is computed on a quarter-annulus region $\Omega = \{0.5 \leq r \leq 1, 0 \leq \theta \leq \frac{\pi}{2}\}$.

Inhomogeneous Dirichlet boundary conditions. We impose inhomogeneous Dirichlet boundary conditions,

$$u(x, t) = \psi(x), \quad x \in \partial\Omega.$$

We consider the heat equation on the unit disk $\Omega = \{x \in \mathbb{R}^2 : |x| < 1\}$,

$$\partial_t u = \kappa \Delta u, \quad x \in \Omega, \quad t \in (0, T],$$

with inhomogeneous Dirichlet boundary conditions

$$u(x, t) = g(x, t), \quad x \in \partial\Omega.$$

We construct an analytic reference solution by restricting a finite linear combination of explicit heat solutions in \mathbb{R}^2 to the disk. Since each component satisfies $\partial_t u = \kappa \Delta u$ in the whole space, the restriction remains an exact source-free solution inside Ω .

Let the shifted heat kernel be defined as

$$G(x, t; x_0, \tau) = \frac{1}{4\pi\kappa(t + \tau)} \exp\left(-\frac{|x - x_0|^2}{4\kappa(t + \tau)}\right), \quad \tau > 0,$$

and denote its spatial derivatives by $\partial_{x_i} G$. We further introduce oscillatory heat modes of the form

$$W_k(x, t) = \exp(-\kappa|k|^2 t) \sin(k \cdot x + \phi),$$

which also satisfy the heat equation in \mathbb{R}^2 .

The reference solution is given by the finite combination

$$\begin{aligned} u_{\text{ref}}(x, t) = & \frac{1}{3} \left(0.9 G(x, t; x_1, \tau_1) - 0.7 G(x, t; x_2, \tau_2) + 0.5 G(x, t; x_3, \tau_3) \right. \\ & + 0.2 \partial_{x_1} G(x, t; x_4, \tau_4) - 0.24 \partial_{x_2} G(x, t; x_4, \tau_4) \\ & - 0.16 \partial_{x_1} G(x, t; x_5, \tau_5) + 0.12 \partial_{x_2} G(x, t; x_5, \tau_5) \\ & \left. + 0.36 W_{k^{(1)}}(x, t) - 0.24 W_{k^{(2)}}(x, t) + 0.16 W_{k^{(3)}}(x, t) \right), \end{aligned}$$

where the parameters are fixed as

$$\begin{aligned} x_1 &= (0.35, -0.15), & \tau_1 &= 1.5, \\ x_2 &= (-0.25, 0.30), & \tau_2 &= 2.0, & k^{(1)} &= (4, 3), \\ x_3 &= (0.05, 0.05), & \tau_3 &= 1.2, & k^{(2)} &= (6, 1), \\ x_4 &= (0.10, -0.35), & \tau_4 &= 1.8, & k^{(3)} &= (2, 5), \\ x_5 &= (-0.40, -0.05), & \tau_5 &= 1.4, \end{aligned}$$

The inhomogeneous Dirichlet boundary data is then defined by restriction,

$$g(x, t) = u_{\text{ref}}(x, t)|_{x \in \partial\Omega},$$

and the initial condition is set as

$$u(x, 0) = u_{\text{ref}}(x, 0).$$

By construction, u_{ref} satisfies $\partial_t u = \kappa \Delta u$ exactly inside Ω , and thus provides a non-separable, non-radial benchmark with time-dependent boundary values.

Homogeneous Neumann boundary conditions. We impose homogeneous Neumann boundary conditions,

$$\partial_n u = 0, \quad x \in \partial\Omega.$$

An analytic reference solution is constructed using eigenfunctions of the Neumann Laplacian on the disk. Let $j_{m,n}$ denote the n -th positive zero of the Bessel function $J_m(z)$, and $j'_{m,n}$ denote the n -th positive zero of the derivative of the Bessel function $J'_m(z)$. The corresponding real-valued Neumann disk harmonics are

$$\psi_{m,n}(r, \theta, t) = J_m(j'_{m,n} r) \cos(m\theta) \exp(-\kappa(j'_{m,n})^2 t).$$

In our experiments, the reference solution is given by the finite-mode combination

$$\begin{aligned} u_{\text{ref}}(r, \theta, t) = & \frac{1}{4} \left(\psi_{0,1}(r, \theta, t) + \frac{1}{4} \psi_{0,2}(r, \theta, t) + \frac{1}{16} \psi_{0,3}(r, \theta, t) + \frac{1}{64} \psi_{0,4}(r, \theta, t) \right. \\ & - \psi_{1,1}(r, \theta, t) - \frac{1}{2} \psi_{1,2}(r, \theta, t) - \frac{1}{4} \psi_{1,3}(r, \theta, t) - \frac{1}{8} \psi_{1,4}(r, \theta, t) \\ & \left. + \psi_{2,1}(r, \theta, t) + \psi_{3,1}(r, \theta, t) + \psi_{4,1}(r, \theta, t) \right). \end{aligned}$$

The initial condition is set as $u(x, 0) = u_{\text{ref}}(x, 0)$, ensuring consistency with the Neumann boundary condition.

Inhomogeneous Neumann boundary conditions. To construct an inhomogeneous Neumann boundary setting, we augment the above reference solution of homogeneous Neumann condition with an additional term

$$\tilde{\psi}(r, \theta, t) = J_1(\lambda_0 r) \cos(\theta) \exp(-\kappa \lambda_0^2 t),$$

where $\lambda_0 = j_{1,1}$ is chosen such that $\tilde{\psi}$ does not satisfy the homogeneous Neumann condition on $r = 1$. The resulting boundary flux is then induced by this term, i.e., $\partial_n u|_{r=1} = \partial_n \tilde{\psi}|_{r=1}$.

Robin boundary conditions. We impose Robin boundary conditions,

$$u + \lambda \partial_n u = 0, \quad x \in \partial\Omega.$$

An analytic reference solution is constructed from a single separable disk harmonic:

$$u_{\text{ref}}(r, \theta, t) = J_2(4r) \cos(2\theta) \exp(-\kappa \cdot 4^2 t).$$

The Robin coefficient λ is chosen such that u_{ref} satisfies the boundary condition at $r = 1$. Imposing $\lambda \partial_n u_{\text{ref}} + u_{\text{ref}} = 0$ yields

$$\lambda = -\frac{J_2(4)}{4J_2'(4)} = \frac{J_2(4)}{4(\frac{1}{2}J_2(4) - J_1(4))},$$

where the final expression uses standard Bessel-function recurrence identities. The initial condition is set as $u(x, 0) = u_{\text{ref}}(x, 0)$.

Mixed boundary conditions. We consider the heat equation on a sectorial annulus

$$\Omega = \{(r, \theta) : r \in [1/2, 1], \theta \in [0, \pi/2]\},$$

which corresponds to a quarter annulus in polar coordinates.

Different types of boundary conditions are imposed on different parts of $\partial\Omega$:

- **Radial boundaries** ($\theta = 0$ and $\theta = \pi/2$): homogeneous Neumann boundary conditions,

$$\partial_\theta u = 0,$$

corresponding to zero flux across the radial edges.

- **Outer circular boundary** ($r = 1$): homogeneous Dirichlet boundary condition,

$$u = 0.$$

- **Inner circular boundary** ($r = 1/2$): inhomogeneous Dirichlet boundary condition,

$$u = g(\theta),$$

where the boundary profile g is induced by the reference solution described below.

This configuration yields a genuinely mixed boundary setting combining Neumann and inhomogeneous Dirichlet constraints on geometrically distinct boundary segments.

An analytic reference solution is constructed using a finite combination of disk harmonics, restricted to the sectorial annulus. Let $j_{m,n}$ denote the n -th positive zero of the Bessel function $J_m(z)$. For integers $m \geq 0$ and $n \geq 1$, define

$$\psi_{m,n}(r, \theta, t) = J_m(j_{m,n} r) \cos(m\theta) \exp(-\kappa j_{m,n}^2 t).$$

The reference solution is given by the finite linear combination

$$\begin{aligned} u_{\text{ref}}(r, \theta, t) = & \frac{1}{4} \left(\psi_{0,1}(r, \theta, t) - \frac{1}{2} \psi_{0,2}(r, \theta, t) + \frac{1}{4} \psi_{0,3}(r, \theta, t) - \frac{1}{8} \psi_{0,4}(r, \theta, t) \right. \\ & + \psi_{2,1}(r, \theta, t) - \frac{1}{2} \psi_{2,2}(r, \theta, t) + \frac{1}{4} \psi_{2,3}(r, \theta, t) - \frac{1}{8} \psi_{2,4}(r, \theta, t) \\ & \left. + \psi_{4,2}(r, \theta, t) \right), \end{aligned}$$

where all modes are evaluated at (r, θ, t) . The initial condition is set as $u(x, 0) = u_{\text{ref}}(x, 0)$.

C.3. Transport Equation

We consider a first-order transport equation on the unit disk

$$\Omega = \{x = (x_1, x_2) \in \mathbb{R}^2 : x_1^2 + x_2^2 \leq 1\}.$$

The scalar field $u(x, t)$ evolves according to

$$\partial_t u + v(x) \cdot \nabla u = 0, \quad x \in \Omega,$$

where the velocity field $v(x)$ is defined by

$$v(x_1, x_2) = (\beta x_1 - x_2, \beta x_2 + x_1),$$

so that the advection operator is $v \cdot \nabla u = (\beta x_1 - x_2) \partial_{x_1} u + (\beta x_2 + x_1) \partial_{x_2} u$. We choose $\beta = 0.2$.

We prescribe a Dirichlet boundary condition on $\partial\Omega$ induced by the reference solution, i.e., $u(x, t) = u_{\text{ref}}(x, t)$ for $x \in \partial\Omega$. The initial condition is set as $u(x, 0) = u_{\text{ref}}(x, 0)$.

The analytic reference solution is constructed by tracing the initial and inflow data along characteristic trajectories. In our experiments, the initial condition u_0 is chosen as the same smooth, non-separable field used in the heat equation benchmark with dirichlet boundary, namely

$$\begin{aligned} u_0(x) = \frac{1}{3} & \left(0.9 G(x, 0; x_1, \tau_1) - 0.7 G(x, 0; x_2, \tau_2) + 0.5 G(x, 0; x_3, \tau_3) \right. \\ & + 0.2 \partial_{x_1} G(x, 0; x_4, \tau_4) - 0.24 \partial_{x_2} G(x, 0; x_4, \tau_4) \\ & - 0.16 \partial_{x_1} G(x, 0; x_5, \tau_5) + 0.12 \partial_{x_2} G(x, 0; x_5, \tau_5) \\ & \left. + 0.36 W_{k^{(1)}}(x, 0) - 0.24 W_{k^{(2)}}(x, 0) + 0.16 W_{k^{(3)}}(x, 0) \right), \end{aligned}$$

is a finite linear combination of shifted heat kernels, their spatial derivatives, and oscillatory modes (see Appendix C.2), and the parameters are fixed as

$$\begin{aligned} x_1 &= (0.35, -0.15), & \tau_1 &= 1.5, \\ x_2 &= (-0.25, 0.30), & \tau_2 &= 2.0, & k^{(1)} &= (4, 3), \\ x_3 &= (0.05, 0.05), & \tau_3 &= 1.2, & k^{(2)} &= (6, 1), \\ x_4 &= (0.10, -0.35), & \tau_4 &= 1.8, & k^{(3)} &= (2, 5). \\ x_5 &= (-0.40, -0.05), & \tau_5 &= 1.4, \end{aligned}$$

Therefore the exact solution of the transport equation can be written in the polar coordinate as

$$u_{\text{ref}}(r, \theta, t) = u_0(r e^{-\beta t}, \theta - t),$$

where u_0 is the prescribed initial condition.

C.4. Burgers Equation

We consider the viscous Burgers equation on the square domain,

$$u_t + u(\partial_{x_1} u + \partial_{x_2} u) = \nu \nabla^2 u, \quad x = (x_1, x_2) \in \Omega = [0, 2\pi]^2.$$

with diffusion coefficient $\nu = 10^{-3}$. Periodic boundary conditions are imposed along both axes:

$$u(x_1 + 2\pi, x_2) = u(x_1, x_2), \quad u(x_1, x_2 + 2\pi) = u(x_1, x_2).$$

The initial condition is defined on the periodic grid as

$$\begin{aligned} u(x_1, x_2, 0) = \frac{1}{100} & \left(\exp(3 \sin x_1 + \sin x_2) + \exp(-3 \sin x_1 + \sin x_2) \right. \\ & \left. - \exp(3 \sin x_1 - \sin x_2) - \exp(-3 \sin x_1 - \sin x_2) \right). \end{aligned}$$

C.5. Baseline Methods and Implementation Details

Physics-Informed Neural Networks (PINNs). As a learning-based baseline, we adopt a standard Physics-Informed Neural Network (PINN) implementation following the setup in prior work (Müller & Zeinhofer, 2023). The solution $u(x, t)$, represented by a neural network, is trained by minimizing a global space–time residual loss, with initial and boundary conditions enforced via additional penalty terms. For the Burgers equation, the same periodic embedding layer as in TENG-BC is used to enforce boundary condition.

Optimization is performed using both BFGS and ENGD algorithm, and each experiment is trained for 100,000 optimization steps. Since (Müller & Zeinhofer, 2023) only provide the implementation for heat equation with dirichlet boundaries, we omit the benchmark of ENGD optimizer for other cases. For all problems, global collocation points are sampled uniformly, with 100,000 interior points, 15,000 initial-condition points, and 10,000 boundary points. The trained PINN solutions are evaluated on the same grids and compared against the same reference solutions using identical error metrics.

Finite Element Method (FEM). As a classical numerical baseline, we implement the finite element method (FEM) based on (Gustafsson & McBain, 2020). For problems defined on rectangular domains (e.g., the Burgers equation), we employ structured square meshes with N^2 grid points, where N denotes the spatial resolution. For circular and other non-rectangular domains, unstructured triangular meshes are used, with an effective spatial resolution set to 256 by default. In all cases, second-order finite elements are adopted for spatial discretization, and second-order time integration schemes are used for temporal discretization. The time step size is fixed to $\Delta t = 10^{-4}$ for all experiments. Boundary and initial conditions are imposed using standard FEM formulations. The FEM solutions are evaluated on the same grids and compared against the same reference solutions as the proposed method.

Spectral method for the Burgers equation. For the Burgers equation with periodic boundary conditions on $[0, 2\pi]^2$, we additionally employ a high-accuracy Fourier spectral method (Canuto et al., 2007) to serve as a numerical reference. The solution is expanded in Fourier modes along both spatial directions, and spatial derivatives are computed in the spectral domain. Time integration is performed using a RK4 time-stepping scheme with a fixed step size $\Delta t = 10^{-4}$. We use a spectral resolution of 1024×1024 Fourier modes, which is sufficient to resolve all relevant scales in the solution. The resulting solution is used for comparison with neural and FEM-based methods under the same evaluation protocol.

D. Additional Experimental Results

Additional numerical visualization results for previous experiments. We first present additional qualitative comparisons between the exact solutions and the solutions obtained by TENG-BC for the heat equation. All TENG-BC solutions shown here are computed using the TENG–Heun time discretization under the default experimental settings. Representative solution snapshots are shown at selected time instances in Figure 5 to Figure 9. The predicted fields produced by TENG-BC closely match the corresponding exact solutions in both global structure and fine-scale details. No spurious oscillations or numerical artifacts are observed throughout the spatial domain. The error remains uniformly small across the domain and does not concentrate near boundaries or regions with higher curvature. This behavior indicates that the boundary-aware formulation in TENG-BC enforces the heat equation and its boundary conditions consistently at each time step, leading to stable and accurate long-term evolution.

We next present the result of transport equation with dirichlet boundary, which poses a more challenging test due to its advection-dominated nature and the absence of intrinsic dissipation. The TENG-BC solutions shown here are computed using the TENG–Heun time discretization under the default experimental settings. Figure 10 compares the exact solution and the TENG-BC prediction at representative time instances. The transported structures are accurately preserved, with both amplitude and phase faithfully reproduced by the neural solver.

We also include the result of Burgers equation with periodic boundary in Figure 11. The TENG-BC solutions shown here are computed using the TENG–Heun time discretization under the default experimental settings. Because of the solution’s shock structure, residual errors are tightly localized along the front, while the remaining regions maintain near-perfect agreement with the spectral reference.

Per-step optimization residuals. In Figure 12, Figure 13 and Figure 14, we report the per-step least-squares residuals of the TENG-BC updates across all benchmark problems. These residuals measure the local fitting accuracy at each time step, reflecting how well the neural representation matches the operator-predicted target under the imposed boundary constraints.

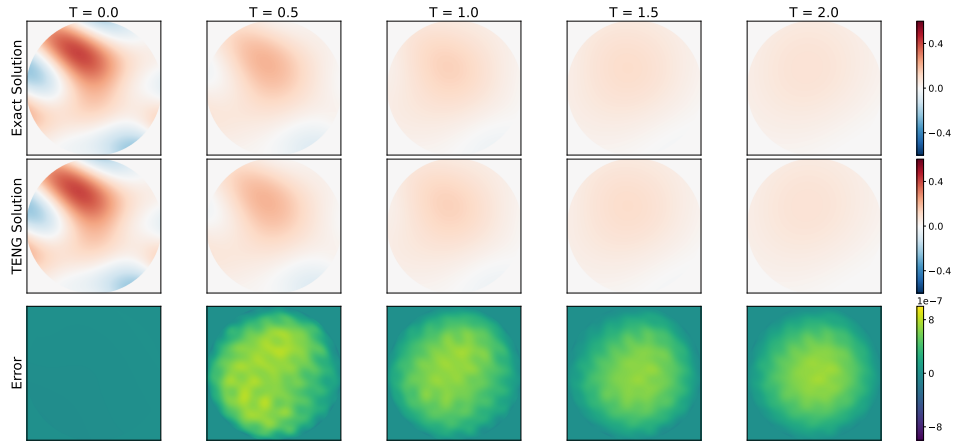


Figure 5. Comparison between the exact solution and the TENG-BC prediction for the heat equation with Dirichlet boundary at representative time instances. Top: exact solution. Middle: solution obtained by TENG-BC. Bottom: absolute error.

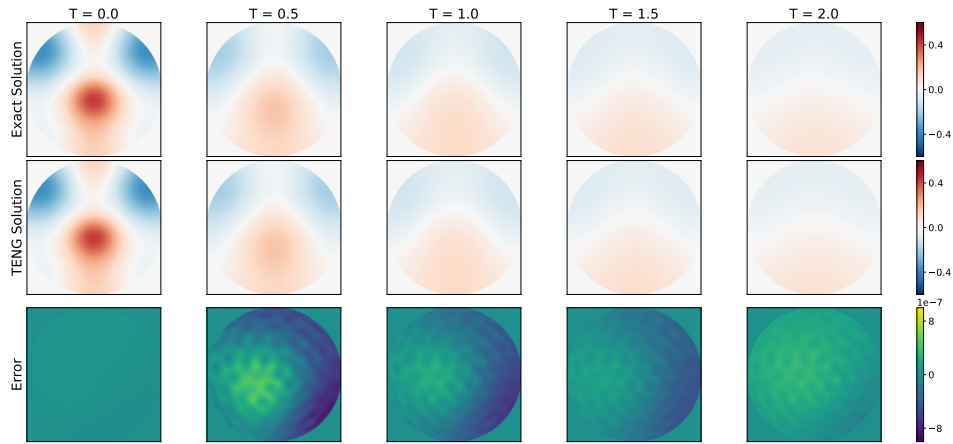


Figure 6. Comparison between the exact solution and the TENG-BC prediction for the heat equation with zero Neumann boundary at representative time instances. Top: exact solution. Middle: solution obtained by TENG-BC. Bottom: absolute error.

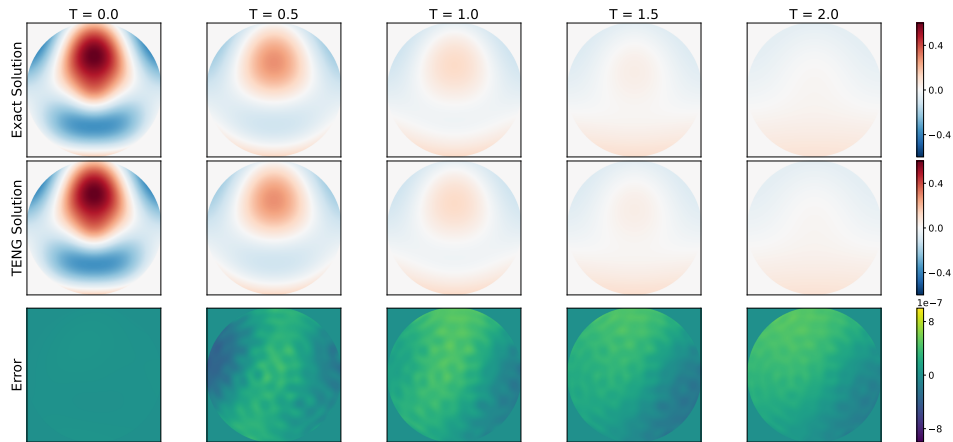


Figure 7. Comparison between the exact solution and the TENG-BC prediction for the heat equation with nonzero Neumann boundary at representative time instances. Top: exact solution. Middle: solution obtained by TENG-BC. Bottom: absolute error.

For heat and transport equations, in all experiments, the residuals remain stable and small throughout the entire temporal evolution, indicating that the boundary-aware least-squares stepper consistently achieves high-precision local updates

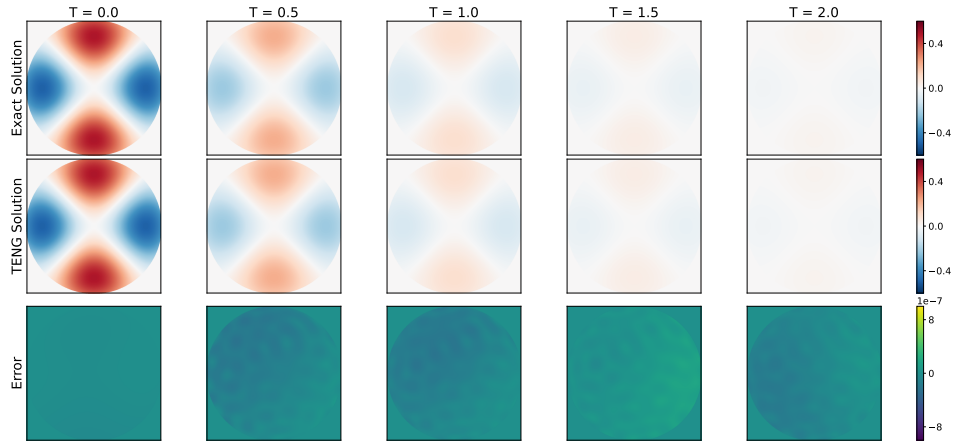


Figure 8. Comparison between the exact solution and the TENG-BC prediction for the heat equation with robin boundary at representative time instances. Top: exact solution. Middle: solution obtained by TENG-BC. Bottom: absolute error.

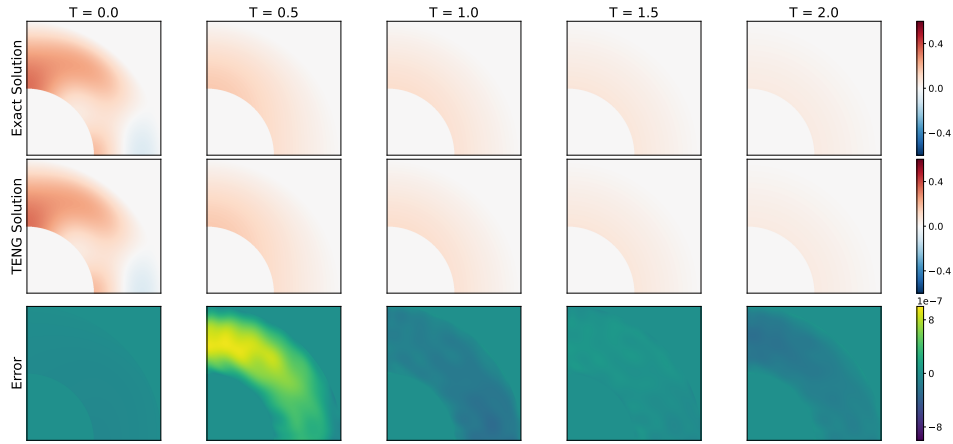


Figure 9. Comparison between the exact solution and the TENG-BC prediction for the heat equation with mixed boundary at representative time instances. Top: exact solution. Middle: solution obtained by TENG-BC. Bottom: absolute error.

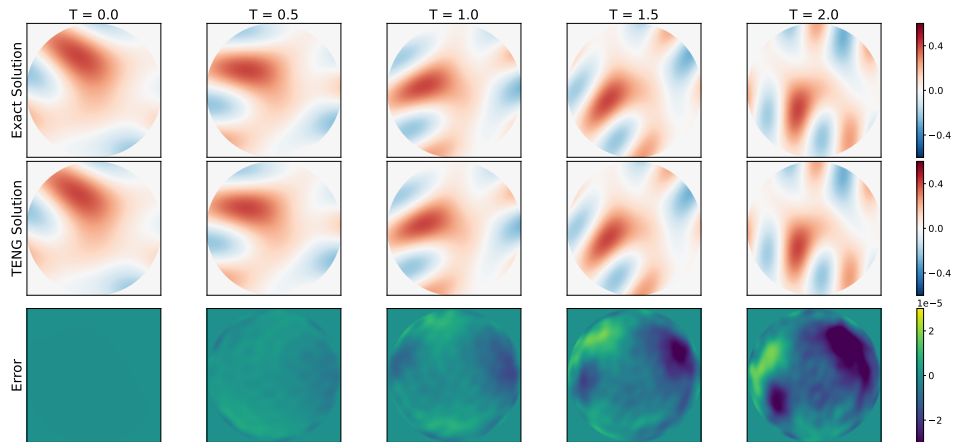


Figure 10. Comparison between the exact solution and the TENG-BC prediction for the transport equation with dirichlet boundary at representative time instances. Top: exact solution. Middle: solution obtained by TENG-BC. Bottom: absolute error.

independent of the underlying PDE type or boundary configuration.

For Burgers equation, The optimization process of TENG-BC reflects the same physical transition as shown by L^2 -error in

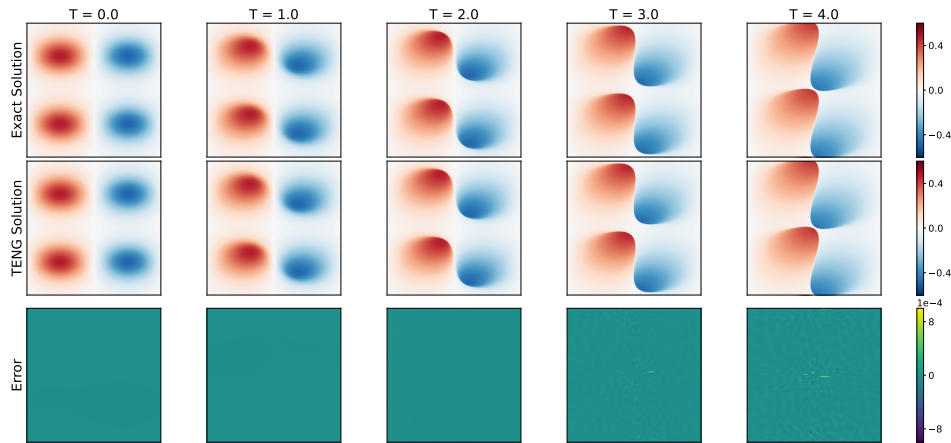


Figure 11. Comparison between the exact solution and the TENG-BC prediction for the Burgers equation with periodic boundary at representative time instances. Top: exact solution. Middle: solution obtained by TENG-BC. Bottom: absolute error.

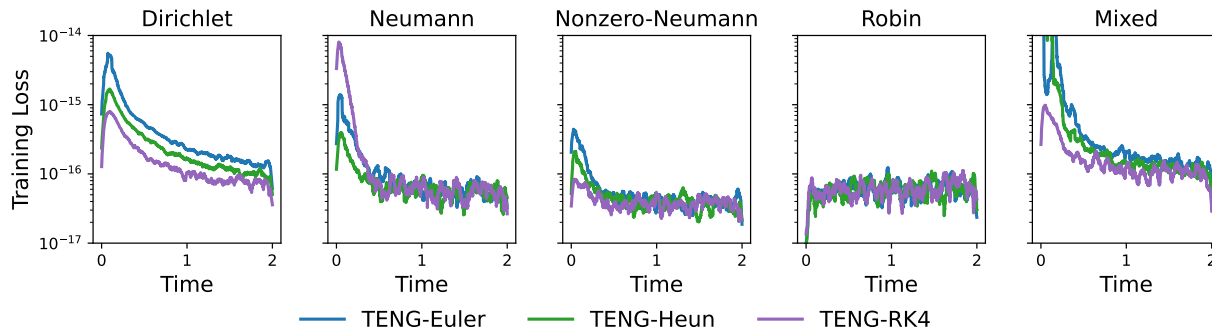


Figure 12. Per-step loss of TENG-BC on the heat equation with different boundaries. Here training loss means the per-step least-squares residuals showing local fitting accuracy within each update.

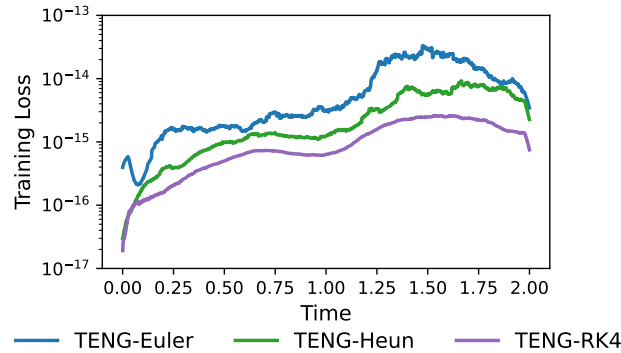


Figure 13. Per-step loss of TENG-BC on the transport equation with dirichlet boundary. Here training loss means the per-step least-squares residuals showing local fitting accuracy within each update.

the main text. In Figure 14, the per-step fitting loss remains near machine precision for most of the evolution, then exhibits a small, well-localized rise around $T \approx 1.8$. This rise coincides with the physical onset of the shock and reflects the increased difficulty of fitting highly non-smooth target functions, rather than a failure of the optimization itself. Importantly, the loss quickly stabilizes afterward, confirming that TENG-BC adapts to the new solution regime without divergence.

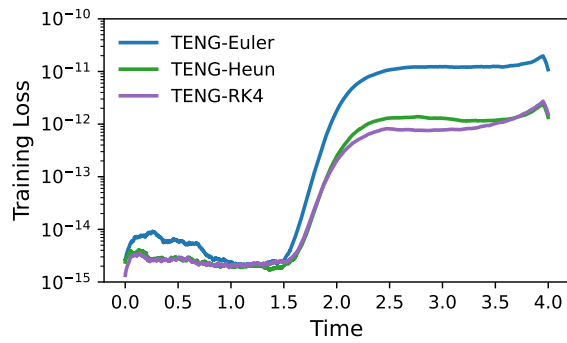


Figure 14. **Per-step loss of TENG-BC on the Burgers equation with periodic boundary.** Here training loss means the per-step least-squares residuals showing local fitting accuracy within each update.